University of Birmingham

Loss Characteristics of TeraHertz Surface Waves on Laser Micromachined Textured Metals

Freer, Suzanna; Qing, Jie; Penchev, Pavel; Dimov, Stefan; Hanham, Stephen M.; Navarro-Cía, Miguel

Document Version
Peer reviewed version

Link to publication on Research at Birmingham portal

Loss Characteristics of TeraHertz Surface Waves on Laser Micromachined Textured Metals

Suzanna Freer, Jie Qing, Pavel Penchev, Stefan Dimov, Stephen M. Hanham, *Senior Member, IEEE* and Miguel Navarro-Cía, *Senior Member, IEEE*

Abstract—For the application of geometrically-induced THz surface wave technology for communication and sensing, a critical analysis of the propagation characteristics (i.e. dispersion and attenuation) for different textured surfaces should be studied and benchmarked. For the broadband characterisation of archetypal textured surfaces (e.g. corrugated plane, two-dimensional array of blind holes and bed of nails) supporting THz transverse magnetic (i.e., p-polarized) surface waves, we employ time-domain spectroscopy and edge-diffraction coupling methods. Measurements of laser micromachined prototypes demonstrate strong frequency-dependent dispersion and the large impact that surface roughness of the order of few μm has on the path loss, increasing it by a factor ranging from 1.6 to 4.3 compared to smooth textured surfaces. Together with numerical modelling, we disentangle all loss mechanisms (namely, ohmic, scattering, propagation divergence and phase mismatch) and highlight the challenge of loss estimation due to surface roughness in highly confined THz surface waves.

Index Terms—Terahertz, time-domain spectroscopy, surface waves, surface roughness.

I. INTRODUCTION

EXTENDING the high field locality and enhancement, as well as slow propagation characteristics of surface plasmons to the TeraHertz (THz) regime requires complex engineering. The high electrical conductivity exhibited by metals at low frequencies, such as THz, means surface plasmons cease to exist and become delocalized Zenneck waves [1]–[3]. To tackle this challenge, one can exploit metamaterial and metasurface design concepts [4], [5] that enable the generation of geometrically-induced surface waves [6], [7] that are sometimes termed spoof surface plasmons [8]–[11]. The tunability of design dimensions grants invaluable control over the dispersion and field locality of these spoof surface plasmons. This ability is useful for the development of THz

S. Freer, J. Qing and M. Navarro-Cía are with the School of Physics and Astronomy, University of Birmingham, Birmingham B15 2TT, United Kingdom (e-mail: M.Navarro-Cia@bham.ac.uk).

J. Qing is also with the School of Electronics and Engineering, University of Electronic Science and Technology, Chengdu, 610056 China.

P. Penchev and S. Dimov are with the Department of Mechanical Engineering, University of Birmingham, Birmingham B15 2TT, United Kingdom.

S. M. Hanham and M. Navarro-Cía are with the Department of Electronic, Electrical and Systems Engineering, University of Birmingham, Birmingham B15 2TT, United Kingdom.
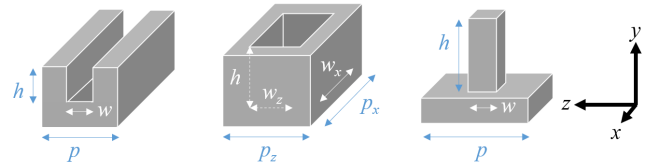
Fig. 1: Unit cell diagrams of the textured platforms: one-dimensional grating, and two-dimensional (2D) rectangular array of blind holes and 2D square array of nails (left to right). The pattern height, width and periodicity is denoted by h, w and p (p_x and p_z for the blind holes), respectively.

TABLE I: Designed and measured unit cell dimensions (in mm) of each structure design. The dimensions were measured using an Olympus measurement microscope, with measurement uncertainty 0.01 mm.

		h	w (x/z)	p (x/z)
Grating	Designed	0.08	0.05	0.10
	Measured	0.08	0.04	0.10
Holes	Designed	0.20	0.21/0.06	0.31/0.16
	Measured	0.14	0.21/0.09	0.31/0.16
Nails	Designed	0.08	0.05	0.10
	Measured	0.09	0.06	0.13

spoof surface plasmons technology from a design standpoint, but brings the concern about fabrication issues such surface roughness. Any of the foreseen applications of THz spoof surface plasmons will struggle to deliver the expected impact due to the limited knowledge of the propagation characteristics, including dispersion and attenuation/path loss [12]–[14], of fabricated prototypes and the lack of effective ways to model unavoidable surface roughness.

Common fabrication techniques for textured surfaces supporting THz spoof surface plasmons include photolithography [14] and silicon micromachining [15], because they surpass conventional computer numerical control milling and 3D printing technology in fabrication accuracy — and surface roughness for the latter [16], [17]. Laser micro-processing is an attractive, non-conventional manufacturing technology suitable for a wide range of micro-components. This is attributed to its intrinsic processing characteristics: (i) non-contact machining that can be used to structure/process a wide range of materials and producing complex free-form (3D) structures that incorporate multi-length scale features with complex geometries; and (ii) in-situ selective machining of free-form surfaces. It therefore shows promise for quality machining when pushed to

micro scales, with the additional advantage of being relatively inexpensive due to cost reduction of laser sources over the last decade. Despite this, laser machining as a fabrication tool remains somewhat unexploited for textured surfaces supporting THz spoof surface plasmons.

The propagation characteristic knowledge gap, including the impact of roughness on the path loss, together with the promise of laser machining, motivates this study that considers three representative textured surfaces. Namely, the structures under investigation are aluminium gratings, arrays of blind holes and arrays of nails (also known as Fakir's bed of nails). The dimensions, presented in Table I, are designed to support a TM surface wave in the range of 0.3 - 0.75 THz, aligned with the frequency of the peak signal of the time-domain spectroscopy (TDS) system used. The periodicity p (p_x and p_z for the blind holes), pattern height h, and width w for each structure are illustrated in Fig. 1. Note that these structures will support leaky-waves for higher frequencies [12], [18], [19].

II. EXPERIMENTAL SET UP

Broadband spoof surface plasmon excitation was achieved through razor blade scattering of the free space wave generated by a photoconductive antenna (PCA), as illustrated in Fig. 2. Here we use the razor blade scheme for coupling despite its low efficiency to allow the propagation loss to be quantified over a wide bandwidth. A significantly more efficient scheme for exciting the surface wave over a narrower bandwidth using a transition from a rectangular waveguide may be found elsewhere [16], [20]. The heights of the razor blades and the angles θ_1 and θ_2 were optimised systematically for each structure by varying them until maximum pulse peak-to-peak amplitude was obtained. The measured waveform is very sensitive to the razor blade height as this height needs to match the out-of-plane confinement of the surface wave [21], which is frequency dependent, for optimum coupling efficiency. The waveform is also sensitive to θ_1 and θ_2, to a lesser extent; θ_1 and θ_2 are significantly different due to the ground effect of the textured surface after the razor blade [22]. The collection section of the setup composed of the receiving antenna and the TPX lens was mounted on the same linear translation stage as the out-coupling razor blade to be able to change d without affecting the out-coupling efficiency. The PCAs are TM-polarized (i.e., E-field is align with the plane of incidence). Details of the PCA radiation and receiving patterns can be found in Ref. [23].

III. RESULTS

A. Fabrication and Topography

Fabrication of the aluminium structures was realised using a state-of-art laser micro-processing system Lasea LS4. Details of the system can be found in Appendix A. The total footprint of the prototypes were 40×40 mm in the xz-plane, see top row in Fig. 3. The three-dimensional profiles of the structures were measured using Focus Variation (FV) technology optical microscope, namely Alicona InfiniteFocus (IF) G5. Profiling measurement details can be found in Appendix B. The 3D profiles of each structure are presented in the bottom row of
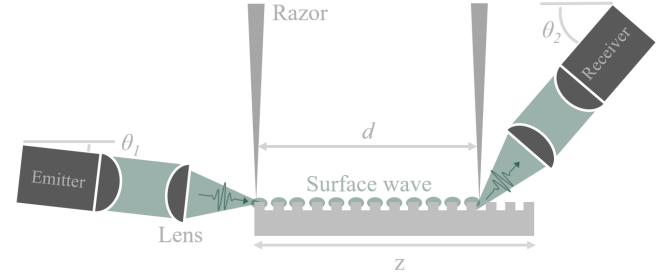

Fig. 2: Illustration of the razor blade coupling scheme. PCAs are used for emission and detection of the terahertz pulses. TPX50 lenses (focal length 50 mm) are used to focus and collect the radiation. The surface wave propagation distance d is defined as the distance between the two razors. The emitting and receiving PCAs are rotated from the horizontal by approximately $\theta_1 = 5°$ and $\theta_2 = 40°$, respectively, for the three textured surfaces

.

Fig. 3. The areal root-mean-square surface roughness extracted from these topographies (with 3,000,000 data points each) is 6.5 μm, 3.0 μm and 6.0 μm for the grating, hole and nail structures, respectively. This information is used later on to model the fabricated rough structures in CST Microwave Studio.

B. Dispersion Characterization

1) Simulation and Analytical Models: The three geometries selected for this study support TM surface modes with different dispersion characteristics. The characteristic spoof surface plasmon frequency (i.e. asymptotic frequency of the dispersion) of modes supported by each geometry was tuned through analytical modelling. Such analytical framework is well-documented in the literature [24]–[26] and it is briefly summarised here for our substrate free structures.

To find the dispersion relation, one must look for the divergence in the reflection coefficient at the interface between air and the textured surface for $k_{||} = k_z$, where $k_{||} > 2\pi f/c_0$ is the component of the wave vector of the incident wave parallel to the top air-metal interface. The dispersion relation for the grating is given by

$$\frac{\sqrt{k_{||}^2 - k_0^2}}{k_0} = \frac{w}{p} \tan(k_0 h), \qquad (1)$$

and for the hole array is given by

$$\frac{\sqrt{k_{||}^2 - k_0^2}}{k_0} = \frac{S^2 k_0}{\sqrt{\pi^2/w_x^2 - k_0^2}} \frac{1 - e^{-2|q_y|h}}{1 + e^{-2|q_y|h}}, \qquad (2)$$

where w, p, h and w_x are geometrical parameters defined in Fig. 2, S is the overlap integral of the plane wave and fundamental mode inside the hole, q_y is the propagation constant $q_y = \sqrt{k_0^2 - \pi^2/w_x^2}$ and k_0 is the free space wavevector.

The dispersion relation for the bed of nails is given by the surface propagation constant
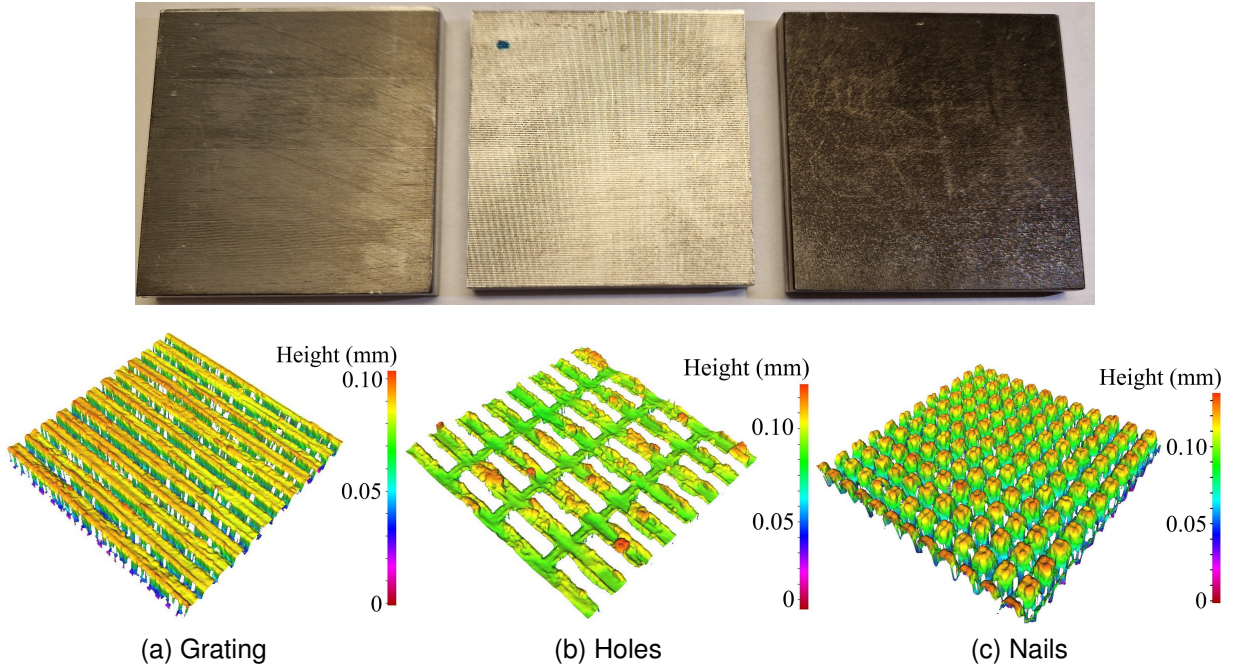
(a) Grating   (b) Holes   (c) Nails

Fig. 3: Prototype pictures along with topographical profiles of the (a) grating, (b) array of holes and (c) array of nails. Note that different colour bars are used to maximise the visualisation of fine details.

(a) Grating   (b) Holes   (c) Nails
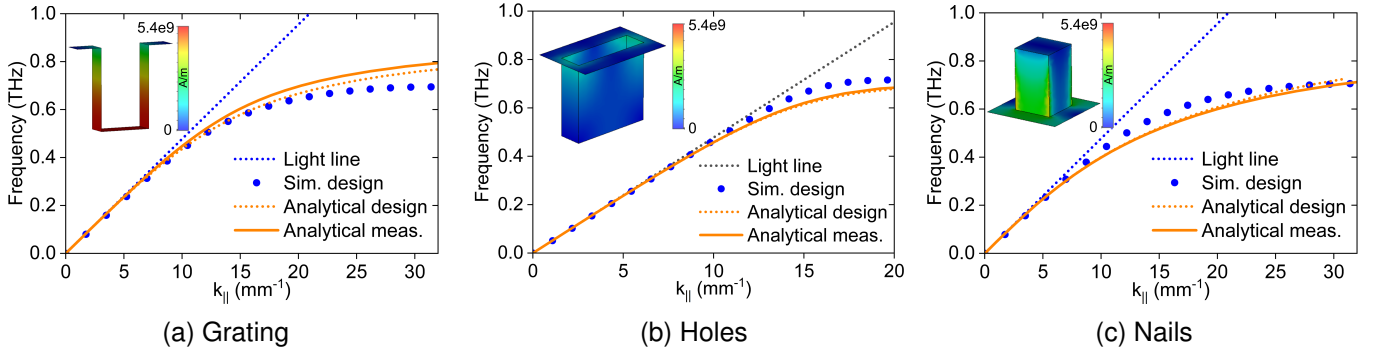
Fig. 4: Simulated (computed in the Eigenmode Solver in CST Microwave Studio) (blue dots) and analytical dispersion diagrams for the (a) grating, (b) array of holes (c) and array of nails, for the designed (dotted orange lines) and measured (solid orange lines) dimensions. Insets: surface currents at the spoof surface plasmon frequency.

$$\gamma = \sqrt{k_p^2 + k_{||}^2 - k_0^2}, \tag{3}$$

where $k_p^2 = \frac{2\pi/p}{\ln(\frac{p}{2\pi w}) + F(r)}$ ($F(r) = 0.5275$ for a square grid [27]).

To determine the robustness of the analytical model of each geometry given the assumptions made, the unit cell of each was modelled using the Eigenmode Solver of CST Microwave Studio, see technical details in Appendix C. The eigenmodes and dispersion relations of each were extracted. Figure 4 presents a comparison of the dispersion for the grating, array of holes and array of nails. One can observe fairly good agreement between the analytical and simulated results, with small deviation close to the frequency cutoff at ∼0.7 THz primarily due to neglecting diffraction [28]; at high

frequencies, the mode is strongly confined and the structure is no longer deeply sub-wavelength.

2) Experiment: The three spoof surface plasmon structures were investigated using THz TDS with razor blade-edge scattering coupling mechanism to enable broadband time-frequency characterisation. Figure 5 presents both the temporal waveform and frequency spectrum of the spoof surface plasmon supported by the grating, array of holes and array of nails of length $d = 20$ mm. To illustrate the temporal response of discrete spectral components, and hence the dispersion of the wave, the spectrogram can be calculated from the waveform, as shown in the figure; see Appendix D for signal processing details. The analytically estimated time of arrival of the different frequency components (computed via the mode group velocity) overlays the spectrogram to facilitate the discussion. One can observe prolonged oscillation of the E-

(a) Grating   (b) Holes   (c) Nails

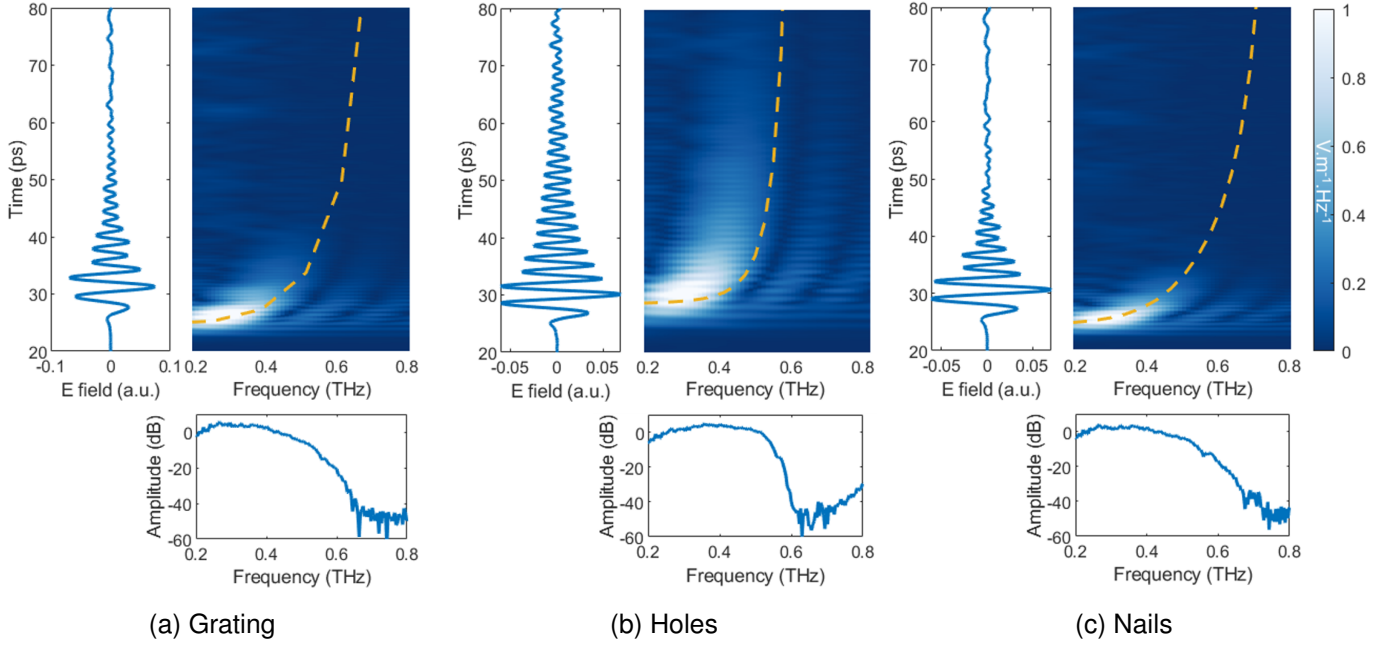Fig. 5: Spectrograms of the absolute value of the transmitted E-field along the (a) grating, (b) array of holes and (c) array of nails. The temporal and frequency responses of each are presented alongside the y and x axes of each spectrogram, respectively. The yellow dashed lines illustrate the dispersion (calculated in CST Microwave Studio for the grating, as the analytical model cannot consider the tapered groove observed in the grating during the profiling study, and analytically calculated for the holes and nails) for the measured structure dimensions found in Table I. Note that a taper angle of $15°$ was used in the grating case to be consistent with the topographical profile.

field in the time domain, a signature of the dispersion of the spoof surface plasmon. The cutoff frequency of each spoof surface plasmon, that is indicated by the rapid drop-off in amplitude in the spectra, differs slightly from the calculated wave dispersion. This is attributed to the decrease in signal amplitude below the sensitivity of the detector for frequency components approaching the spoof surface plasmon frequency as these frequency components experience increased attenuation. One can also observe consistency between the analytical and measured dispersion of the spoof surface plasmons. When performing a comparison of the different structures, the array of holes exhibits a sharper frequency cutoff than the grating and array of nails, consistent with simulation and analytical models that show a narrower surface wave (i.e. $k_{||} >> 2\pi f/c_0$) bandwidth. Figure 5 also shows that the structures support single mode propagation, enabling attenuation calculation straightforwardly as detailed next. The single mode propagation and trapped nature are further confirmed by simulations found in Appendix C.

C. Path loss

The power attenuation (i.e., absorption) of a surface wave is often measured using a cutback-like method whereby

$$\alpha = -\frac{\ln\left(|E(f)_{D2}|^2/|E(f)_{D1}|^2\right)}{d}, \qquad (4)$$

where $E(f)_D$ is the E-field amplitude at position D along the structure and d is the difference between two positions $D1$

and $D2$. The second (detecting) razor blade edge is positioned at two different distances along the structure ($D1$ and $D2$), while maintaining its separation with respect to the top of the textured surface, and the transmitted E-field is measured for each. This approach, however, actually computes what is known in telecommunications as power path loss. Any spoof surface plasmon or Zenneck wave propagating in an all-metallic textured platform suffer from ohmic, α^{ohmic}, and scattering (due to surface roughness) losses, α^{scatt}, that represent attenuation as commonly understood, and propagation divergence (i.e., in-plane spreading) represented through the E-field path loss exponent, ζ, that results in an effective loss of signal strength at the detector end. Note that for a wave propagating cylindrically in an isotropic xz surface, the E-field can be formulated as $E = \frac{1}{\sqrt{\rho}}Ae^{-j(k_{||}-j\alpha)\rho}$, where A is an amplitude, and $\rho = \sqrt{x^2 + z^2}$; hence, ζ is 0.5, and thus, the power path loss is 1. The omission of distinguishing attenuation and path loss in the literature of THz surface waves renders concerns regarding the few reported measured attenuation values [12], [21], [29]–[32] and can explain the still unresolved discrepancy in terms of propagation length between measurements and theory [33], [34]. In addition, despite the expected significant impact of roughness in the attenuation of the THz surface waves and thus in the path loss, no study has been carried out until now to the best of our knowledge. Note that the x dimension is chosen to be large enough such that reflections from edges have an arriving delay time exceeding the recorded time delay window, and thus, are not present in

the measurement.

Figure 6 presents the experimental path loss of the spoof surface plasmon supported by each of the three geometries, calculated using Eq. 4. The frequency range is truncated at 0.6 THz since beyond this frequency the signal falls below the noise level of the system for all geometries. The transmission was measured for five razor blade separations; namely, $d = 22$, 27, 32, 37, and 42 mm. This allows us to have ten separation combinations, and thus, ten estimates of the attenuation. The detection razor and PCA were moved simultaneously. The shaded regions in the figure illustrate the standard deviation from all ten combinations of measurements. The path loss of all spoof surface plasmons increases with frequency due to the higher spoof surface plasmon confinement and the smaller group velocity of the higher frequency components. The former characteristic amplifies the effect of scattering due to surface roughness, whereas the latter characteristic leads to longer interaction time between the spoof surface plasmon and the metal, yielding higher ohmic loss. The fact that the array of nails has the highest power attenuation is consistent with the simulated dispersion relations presented in Fig. 4. Therein, the wavevector for the nail geometry deviates the furthest from the light line in the frequency range of the surface wave condition, although marginally compared to the grating. This results in higher E-field confinement as demonstrated in Appendix C, and hence higher power attenuation. The power attenuation of the array of holes falls between the other two platforms unexpectedly if considering the dispersion relations and the surface currents depicted as insets in Fig. 4 wherein the array of holes display the lowest field confinement and the lowest surface current. This unexpected moderate power attenuation is arguably due to the higher propagation divergence as demonstrated in the next paragraphs, the highly resonant nature (illustrated in Appendix C through the Q factor) and strong hole size dependence of its dispersion; small geometry deviations on the hole size due to roughness smear out the dispersion dramatically, leading to phase matching losses as well as scattering losses that are difficult to model. The sudden drop for the nail prototype at 0.6 THz is attributed to the earlier vanishing signal. For instance, for d = 20 mm the nail signal vanishes beyond 48 ps (see Fig. 5(c)); the measurement hits the noise floor of the setup at that time delay that corresponds to ∼0.6 THz. All d considered here are larger than 20 mm, so noise floor is expected to be reached earlier than 0.6 THz for the nails.

Eigenmode calculations in one dimension, in addition to 2D full-wave simulations (technical details and results for the grating can be found in Appendix C), neglect propagation divergence. Two-dimensional simulations do not capture the in-plane spreading of the spoof surface plasmon as it propagates, and as such, they compute attenuation, not path loss. To disentangle all the contributions to the path loss, namely ohmic, scattering and spreading loss, we run 2D and 3D simulations (we refer the reader to Appendix C to understand the methodology to compute the different attenuation contributions independently) whose results for the corresponding attenuation coefficients α_{sim}^{ohmic} and α_{sim}^{scatt}, and E-field path loss exponent ζ are plotted in Fig. 7. It is worth noting the
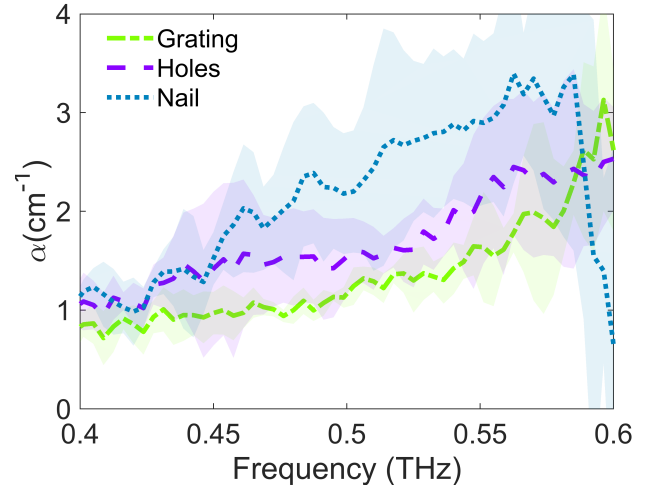

Fig. 6: THz spoof surface plasmon power path loss for a grating, array of holes, and array of nails. The shaded regions denote the standard deviation of the measurements. The drop experienced by the nails at the top end of the spectral window is likely an artifact due to measurement limitations.

large ζ for the holes; this is because the corresponding spoof surface plasmon is only truly developed closer to 0.6 THz as shown in Appendix C; for lower frequencies, the wave is better described as an untrapped wave propagating in a nearly smooth metal plane. We also compute the attenuation (2D model) and path loss (3D model) with the Hammerstad-Jensen model of defining an effective conductivity to account for roughness [35] ($\alpha_{sim}^{eff.cond.}$); this approach is a built-in function in CST Microwave Studio and enables us to assess its validity in the context of THz surface waves. The results at three relevant frequencies are tabulated in Table II.

Figure 7 and Table II demonstrate how α_{meas} reconciles very well with simulations for the grating and nails and reasonably well for holes when adding together α_{sim}^{ohmic}, α_{sim}^{rough} and ζ. The frequency increasing underestimation of the simulated average path loss compared to the average measured path loss for the holes (yet within error shaded regions) is arguably bridged by the phase mismatch loss elucidated earlier, but it could also be due to simulation limitations that underestimate α_{sim}^{ohmic} and α_{sim}^{rough}; the highly resonant nature of the holes poses a challenge for time-domain simulations. Figure 7 and Table II also highlight that the common practice of assigning an effective conductivity to a metal to account for roughness (i.e., $\alpha_{sim}^{eff.cond}$ case) breaks down for spoof surface plasmons. Depending on the surface texture, this approach to account for scattering loss without mapping the roughness can under- or over-estimate the path loss. Hence, for an accurate estimate of the attenuation of spoof surface plasmons, it is imperative to physically model the roughness.

IV. SUMMARY

The propagation characteristics of three geometrically-induced THz surface waves (i.e., spoof surface plasmons) have been systematically studied and benchmarked with a combined analytical, experimental and computational approach. The
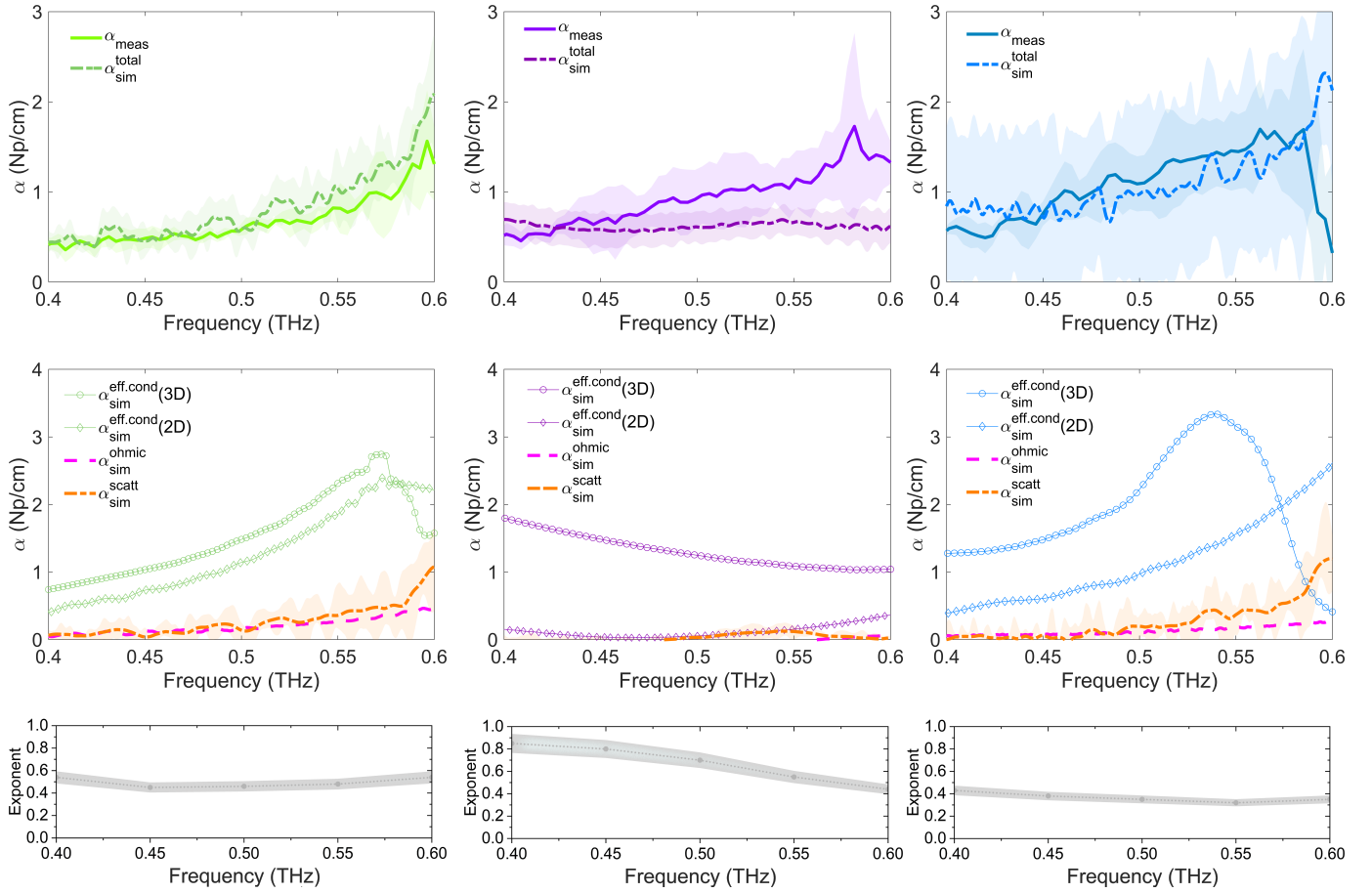
Fig. 7: (Top row) Measured (α_{meas}) and simulated (α_{sim}^{total}) THz spoof surface plasmon E-field path loss, (middle row) simulated attenuation coefficient $\alpha_{sim}^{eff.cond.}$, α_{sim}^{ohmic}, and α_{sim}^{scatt}, and (bottom row) E-field path loss exponent ζ associated to in-plane spreading for the (left) grating, (middle) array of holes and (right) array of nails. Measured and modelled surface roughness (root-mean-square) was 6.5 µm, 3.0 µm and 6.0 µm for the grating, array of holes and array of nails, respectively. The drop experienced by the nails at the top end of the spectral window is likely an artifact due to measurement limitations. The shaded regions illustrate the standard deviation of the results.

TABLE II: Measured (α_{meas}) path loss, simulated attenuation coefficient ($\alpha_{sim.2D}^{eff.cond}/\alpha_{sim}^{ohmic}/\alpha_{sim}^{scatt}$) and E-field path loss exponent (ζ) of the grating, array of holes, and array of nails at multiple frequencies. Negative values in α_{sim}^{ohmic} and α_{sim}^{scatt} are nonphysical and are due to numerical error.

Platform	Freq (THz)	$\alpha_{meas}(Np/cm)$	$\alpha_{sim.2D}^{eff.cond}(Np/cm)$	$\alpha_{sim}^{ohmic}(Np/cm)$	$\alpha_{sim}^{scatt}(Np/cm)$	ζ
Grating	0.4	0.43 ± 0.11	0.37	0.05	0.10 ± 0.10	0.54 ± 0.05
	0.5	0.56 ± 0.05	1.18	0.19	0.31 ± 0.15	0.46 ± 0.05
	0.6	1.31 ± 0.41	2.17	0.52	1.63 ± 0.69	0.54 ± 0.05
Holes	0.4	0.53 ± 0.13	0.14	-0.01	-0.04 ± 0.08	0.85 ± 0.09
	0.5	0.92 ± 0.33	0.07	-0.11	-0.00 ± 0.04	0.70 ± 0.07
	0.6	1.33 ± 0.24	0.37	0.04	0.09 ± 0.02	0.44 ± 0.04
Nails	0.4	0.60 ± 0.06	0.40	-0.08	0.14 ± 0.12	0.45 ± 0.04
	0.5	1.09 ± 0.31	0.97	0.17	0.32 ± 0.17	0.35 ± 0.03
	0.6	0.32 ± 1.01	2.52	0.34	1.40 ± 0.38	0.36 ± 0.03

textured platforms under investigation fabricated by laser micromachining have been a one-dimensional corrugated metal plane, a 2D rectangular array of blind holes and a 2D square array of nails. The key concept of path loss used in free-space radio and wireless communication system has been introduced to spoof surface plasmons to make a clear distinction between spoof surface plasmon path loss and spoof surface plasmon attenuation, and to explain the disagreement between measurements and calculations in the literature of THz surface waves. Particular focus has been on the impact of surface roughness in the path loss of spoof surface plasmons, highlighting the unsuitability of modelling conductor surface roughness through an effective conductivity (that is common practice) for spoof surface plasmons. The work provides key missing information for designers of spoof surface plasmon applications in sensing and communications [36], [37] domains.
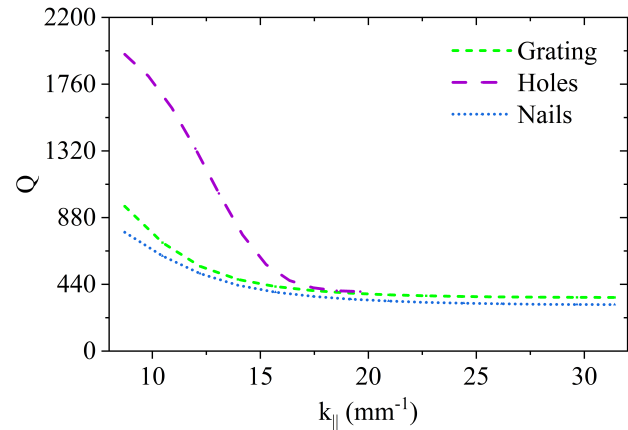

Fig. 8: Q-factor of the grating (orange), array of holes (red) and array of nails (blue) THz spoof surface plasmons.

APPENDIX A
FABRICATION DETAILS

The fabrication was realized on a state-of-art laser microprocessing system Lasea LS4. The system integrates a stack of five mechanical axes for orienting the workpiece in relation the laser beam, where the three linear stages have a position resolution of 0.25 μm, while the two rotary stages possess a position resolution of 45 μrad. The laser system is equipped with 3D optical scan head, allowing to achieve maximum laser beam stirring speeds of 5 m/s, while the achievable positional accuracy and precision are better than ±5 μm across the full range of scanning speeds. The laser system integrates an Yb-doped ultrafast (ps/fs) 10W laser sources from Amplitude Systemes that operates at a central wavelength of 1030 nm, and has a pulse duration in the range of 310 fs - 10 ps and maximum pulse repetition rate of 2 MHz. The utilization of the fs laser source in the experiments allows to minimise the heat-affected zone around the processed area and thus to reduce the thermally induced cracks and damages. At the same time the optical axes are employed to realize the required laser beam movements on the work-piece in order to benefit from the high scanning speeds of the optical galvanometer scanner (up to 5 m/s) and thus to obtain high machining throughputs. Table III summarizes the predetermined laser parameter settings used for the laser processing trials.

TABLE III: Optimized laser parameter settings used for the laser processing trials.

Laser parameter	Value
Power	7 W
Frequency	100 kHz
Pulse energy	70 μJ
Scanning speed	0.5 m/s
Pulse duration	310 fs
Laser beam polarisation	Circular
Hatch style	Random
Hatch pitch	4 μm
Ablation rate per layer	5 μm

APPENDIX B
PROFILING MEASUREMENT DETAILS

Measurement characterization of laser manufactured geometries in terms of accuracy, repeatability and reproducibility is performed with FV technology optical microscope, namely Alicona IF G5. It is equipped with x5, x10, x20, x50 objective and x100 lenses that provide lateral resolution of 3.52 μm, 1.76 μm, 0.88 μm, 0.64 μm and 0.44 μm and vertical resolution of 0.41 μm, 0.1 μm, 0.05 μm, 0.02 μm and 0.01 μm, respectively. The system is equipped with three mechanical axes with travel range of 100 mm in X, Y and Z axes for measurement envelopes bigger than the field of view of the objective lenses. The measurement repeatability of the system is 0.12 μm, 0.03 μm, 0.01 μm, 0.003 μm and 0.001 μm for x5, x10, x20, x50 and x100 objective lenses, respectively. The system also has a set of software tools (MeasureSuite), which allow analyses of measurement data both in terms of form and surface topography. All analyses conform to the relevant ISO standards: profile roughness and surface texture analyses conform to ISO 4287/4288 and 3D form analyses conform to the ISO 1101.

APPENDIX C
SIMULATION DETAILS

The Eigenmode and Transient Solvers of CST Microwave Studio were used to simulate the response of the corrugated platforms.

Dispersion diagram: in the Eigenmode Solver, periodic boundary conditions were implemented for the unit cell in the z-direction for the grating geometry and x- and z-directions for the hole and nail geometry. Electric walls were defined in the y direction and magnetic walls were defined in the x direction for the grating geometry. To compute the Q-factor (see Fig. 8), the General (lossy) method is used.

Attenuation study: in the Transient Solver, the platforms (with a total length in z of 50 mm) and excitation were modelled as 2D (i.e., invariant along x), except for the calculation of the ζ where the fabricated prototype was modelled, see Fig. 9. For the 2D simulations, solver-defined open add space
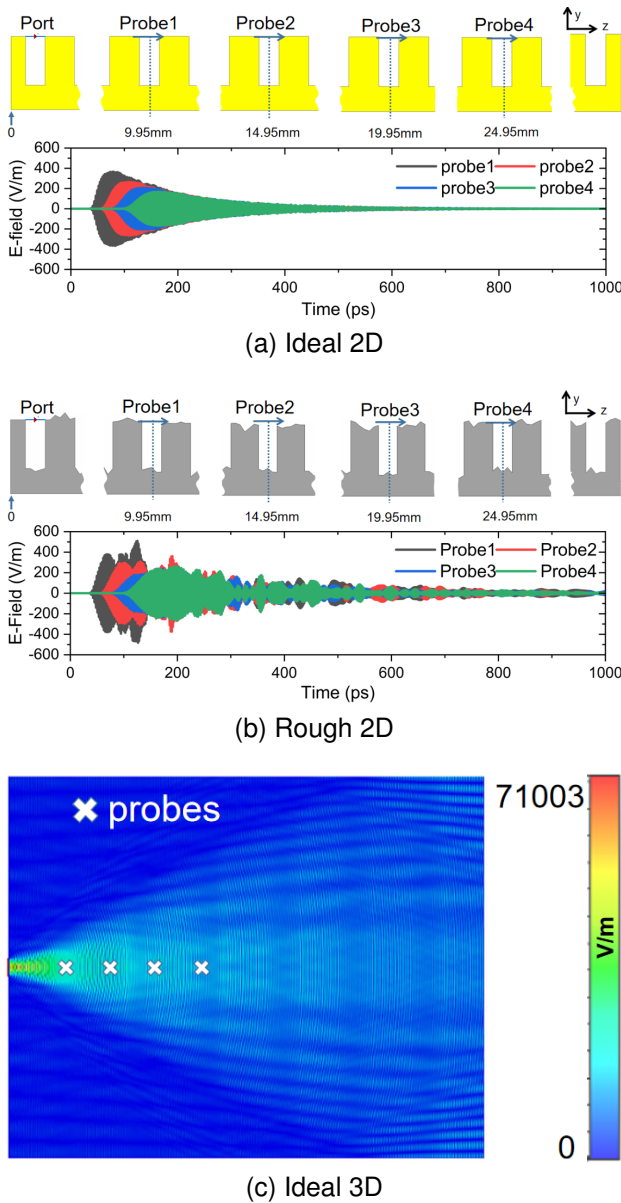
This article has been accepted for publication in IEEE Transactions on Terahertz Science and Technology. This is the author's version which has not been fully edited and content may change prior to final publication. Citation information: DOI 10.1109/TTHZ.2024.3358738

JOURNAL OF LATEX CLASS FILES, VOL. XX, NO. YY, APRIL 2023   8

(a) Ideal 2D

(b) Rough 2D

(c) Ideal 3D

Fig. 9: Set of simulation results to compute α_{sim}^{total}: (a) E-field at different positions on an ideal 2D grating model for α_{sim}^{ohmic} calculation, (b) E-field at different positions on a rough 2D grating model for α_{sim}^{scatt}, and (c) $|E(x,z)|$-field at 0.5 THz on the top interface of an ideal 3D grating model for ζ. Position of the E-field probes are explicitly indicated in the three panels.

boundary conditions were set in y and z, with magnetic walls in x. For the 3D simulations (i.e., the fabricated prototype) to compute ζ, solver-defined open add space boundary conditions were set in all directions. The metal was modelled as aluminium, with conductivity $\sigma = 3.56 \times 10^7$ S/m (to compute α_{sim}^{ohmic}, see Fig. 9(a)), or with a lower conductivity (to compute $\alpha_{sim.2D}^{eff.cond}$ and $\alpha_{sim.3D}^{eff.cond}$), and as perfect electric conductor (to compute α_{sim}^{scatt} and ζ, see Fig. 9(b,c), respectively). For the surface roughness impact study, two types of simulations were run: one using a CST Microwave Studio macro which uses the Hammerstad-Jensen model to describe the effect of surface roughness on the conductivity [35], and
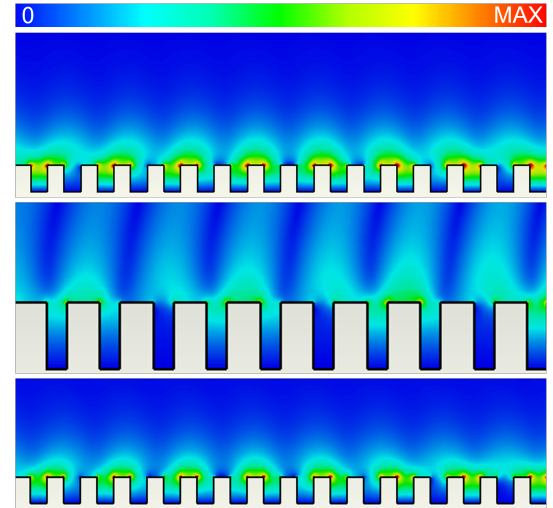

Fig. 10: $|E(y,z)|$-field at 0.6 THz for the (top) grating, (middle) array of holes and (bottom) array of nails.

one where the top and bottom interfaces of the texture surfaces are random rough surfaces and metal is modelled as perfect electric conductor (see Fig. 9(b)). To create the latter, one-dimensional random surfaces were generated in MATLAB with a Gaussian height distribution function matching the measured root-mean-square surface roughness and a Gaussian autocovariance function with correlation length of 0.01 mm. These were imported into CST and extruded along x. Note that no roughness is introduced on the vertical walls due to computational burden. To map accurately the rough surface within our computational resources, a fine hexahedral mesh of 2 μm × 2 μm was used. Simulations were stopped when the remaining energy in the simulation was 80 dB and 20 dB below the peak value for the 2D and 3D cases, respectively. The simulated attenuation was extracted using Eq. 4 divided by 2 (to convert power attenuation to attenuation coefficient) – after Fourier transformation of the waveforms shown in Fig. 9 – with all possible combinations from 4 probes spaced 5 mm between each other whose precise positions in the simulation are indicated in Fig. 9. To compute ζ, the z component of E-field was recorded at different frequencies over the xz-plane right above the textured surface and its decay along z-direction was fitted with a function of the form $\frac{1}{z^\zeta}$.

Field distribution: the E-field on the yz-plane were extracted from the 2D simulation used to compute α_{sim}^{ohmic} to visualise the surface wave nature of the electromagnetic modes supported by the corrugated platforms in the spectral window under investigation, see Fig. 10. In agreement with the dispersion diagrams, grating and array of nails support more confined spoof surface plasmons than the array of holes.

APPENDIX D
DATA PROCESSING

The spectrograms in Fig. 5 were calculated using short-time Fourier transformation of the time-domain signal. The overlap was defined as 98% of the zero-padding length and the number of DFT points was 512.

This article has been accepted for publication in IEEE Transactions on Terahertz Science and Technology. This is the author's version which has not been fully edited and content may change prior to final publication. Citation information: DOI 10.1109/TTHZ.2024.3358738

JOURNAL OF LATEX CLASS FILES, VOL. XX, NO. YY, APRIL 2023   9

REFERENCES

[1] A. Ishimaru, *Electromagnetic Wave Propagation, Radiation, and Scattering*. Hoboken, NJ, USA: John Wiley & Sons, Inc., 2017.

[2] T.-I. Jeon and D. Grischkowsky, "Thz zenneck surface wave (thz surface plasmon) propagation on a metal sheet," *Applied Physics Letters*, vol. 88, no. 6, p. 061113, 2006.

[3] M. Navarro-Cía, M. Natrella, F. Dominec, J. C. Delagnes, P. Kužel, P. Mounaix, C. Graham, C. C. Renaud, A. J. Seeds, and O. Mitrofanov, "Terahertz imaging of sub-wavelength particles with zenneck surface waves," *Applied Physics Letters*, vol. 103, no. 22, p. 221103, 2013.

[4] E. Martini, M. Mencagli, and S. Maci, "Metasurface transformation for surface wave control," *Philosophical Transactions of the Royal Society A: Mathematical, Physical and Engineering Sciences*, vol. 373, no. 2049, 2015.

[5] J. S. Gomez-Diaz and A. Alù, "Flatland optics with hyperbolic metasurfaces," *ACS Photonics*, vol. 3, no. 12, pp. 2211–2224, 2016.

[6] R. S. Elliott, "On the theory of corrugated plane surfaces," *Transactions of the IRE Professional Group on Antennas and Propagation*, vol. 2, no. 2, pp. 71–81, 1954.

[7] A. F. Harvey, "Periodic and Guiding Structures at Microwave Frequencies," *IRE Transaction on Microwave Theory and Techniques*, pp. 30–61, 1960.

[8] M. Navarro-Cía, M. Beruete, S. Agrafiotis, F. Falcone, M. Sorolla, and S. A. Maier, "Broadband spoof plasmons and subwavelength electromagnetic energy confinement on ultrathin metafilms," *Opt. Express*, vol. 17, no. 20, pp. 18 184–18 195, Sep 2009.

[9] P. A. Huidobro, A. I. Fernández-Domínguez, J. B. Pendry, L. Martín-Moreno, and F. J. García-Vidal, *Spoof Surface Plasmon Metamaterials*. Cambridge University Press, 2018.

[10] H. Feng Ma, X. Shen, Q. Cheng, W. Xiang Jiang, and T. Jun Cui, "Broadband and high-efficiency conversion from guided waves to spoof surface plasmon polaritons," *Laser and Photonics Reviews*, vol. 8, no. 1, pp. 146–151, 2014.

[11] Z. Ma, S. M. Hanham, P. Arroyo Huidobro, Y. Gong, M. Hong, N. Klein, and S. A. Maier, "Terahertz particle-in-liquid sensing with spoof surface plasmon polariton waveguides," *APL Photonics*, vol. 2, no. 11, p. 116102, 2017.

[12] R. Ulrich, "Modes of propagation on an open periodic waveguide for the far infrared," in *Symposium on Optical and Acoustical Micro-Electronics*, Jan. 1974, pp. 359–376.

[13] W. Zhu, A. Agrawal, A. Cui, G. Kumar, and A. Nahata, "Engineering the propagation properties of planar plasmonic terahertz Waveguides," *IEEE Journal on Selected Topics in Quantum Electronics*, vol. 17, no. 1, pp. 146–153, 2011.

[14] B. Ng, S. M. Hanham, J. Wu, A. I. Fernández-Domínguez, N. Klein, Y. F. Liew, M. B. Breese, M. Hong, and S. A. Maier, "Broadband Terahertz Sensing on Spoof Plasmon Surfaces," *ACS Photonics*, vol. 1, no. 10, pp. 1059–1067, 2014.

[15] D. González-Ovejero, C. Jung-Kubiak, M. Alonso-delPino, T. Reck, and G. Chattopadhyay, "Design, fabrication and testing of a modulated metasurface antenna at 300 ghz," in *2017 11th European Conference on Antennas and Propagation (EUCAP)*, 2017, pp. 3416–3418.

[16] S. Freer, R. Martínez, D. Pérez-Quintana, M. Beruete, S. M. Hanham, M. M. Attallah, and M. Navarro-Cía, "Metal 3d printed d-band waveguide to surface wave transition," in *2020 45th International Conference on Infrared, Millimeter, and Terahertz Waves (IRMMW-THz)*, 2020, pp. 1–2.

[17] A. M. Mohammed, Y. Wang, T. Skaik, S. Li, and M. Attallah, "Conductivity measurement using 3d printed re-entrant cavity resonator," *Measurement Science and Technology*, vol. 33, no. 5, p. 055017, Feb 2022.

[18] A. A. Oliner, "Radiating periodic structures: analysis in terms of k versus β diagrams," in *Short Course on Microwave Field and Network Techniques, Polytechnic Institute of Brooklyn*, June 1963.

[19] R. E. Collin and F. J. Zucker, *Antenna Theory: part 2*, ser. Interuniversity electronics. New York, USA: McGraw-Hill, 1969, vol. 7.

[20] C. H. Walter, *Traveling Wave Antennas*. Los Altos, CA, USA: Peninsula Publishing, 1990.

[21] J. Saxler, J. Gómez Rivas, C. Janke, H. P. M. Pellemans, P. H. Bolívar, and H. Kurz, "Time-domain measurements of surface plasmon polaritons in the terahertz frequency range," *Phys. Rev. B*, vol. 69, p. 155427, Apr 2004.

[22] C. A. Balanis, *Antenna Theory: Analysis and Design*. Hoboken, NJ, USA: John Wiley & Sons, Inc., 2005.

[23] S. Freer, A. Gorodetsky, and M. Navarro-Cía, "Beam Profiling of a Commercial Lens-Assisted Terahertz Time Domain Spectrometer," *IEEE Transactions on Terahertz Science and Technology*, vol. 11, no. 1, pp. 90–100, 2021.

[24] F. J. Garcia-Vidal, L. Martín-Moreno, and J. B. Pendry, "Surfaces with holes in them: new plasmonic metamaterials," *Journal of Optics A: Pure and Applied Optics*, vol. 7, no. 2, p. S97, 2005.

[25] S. Papantonis, S. Lucyszyn, and E. Shamonina, "Dispersion effects in fakir's bed of nails metamaterial waveguides," *Journal of Applied Physics*, vol. 115, p. 054903, 2014.

[26] M. G. Silveirinha, C. A. Fernandes, and J. R. Costa, "Electromagnetic characterization of textured surfaces formed by metallic pins," *IEEE Transactions on Antennas and Propagation*, vol. 56, no. 2, pp. 405–415, 2008.

[27] P. A. Belov, R. Marques, S. Maslovski, I. Nefedov, M. Silverinha, C. Simovski, and S. Tretyakov, "Strong spatial dispersion in wire media in the very large wavelength limit," *Physical Review B*, vol. 67, p. 113103, 2003.

[28] E. Hendry, A. P. Hibbins, and J. R. Sambles, "Importance of diffraction in determining the dispersion of designer surface plasmons," *Physical Review B*, vol. 78, no. 23, p. 235426, dec 2008.

[29] K. W. Steijn, R. J. Seymour, and G. I. Stegeman, "Attenuation of far-infrared surface plasmons on overcoated metal," *Applied Physics Letters*, vol. 49, no. 18, pp. 1151–1153, 1986.

[30] C. R. Williams, S. R. Andrews, S. A. Maier, A. I. Fernández-Domínguez, L. Martín-Moreno, and F. J. García-Vidal, "Highly confined guiding of terahertz surface plasmon polaritons on structured metal surfaces," *Nature Photonics*, vol. 2, no. 3, pp. 175–179, 2008.

[31] C. R. Williams, M. Misra, S. R. Andrews, S. A. Maier, S. Carretero-Palacios, S. G. Rodrigo, F. J. Garcia-Vidal, and L. Martin-Moreno, "Dual band terahertz waveguiding on a planar metal surface patterned with annular holes," *Applied Physics Letters*, vol. 96, no. 1, p. 011101, 2010.

[32] S. Pandey, B. Gupta, A. Chanana, and A. Nahata, "Non-drude like behaviour of metals in the terahertz spectral range," *Advances in Physics: X*, vol. 1, no. 2, pp. 176–193, 2016.

[33] D. Begley, R. Alexander, C. Ward, R. Miller, and R. Bell, "Propagation distances of surface electromagnetic waves in the far infrared," *Surface Science*, vol. 81, no. 1, pp. 245–251, 1979.

[34] V. V. Gerasimov, B. A. Knyazev, A. K. Nikitin, and G. N. Zhizhin, "A way to determine the permittivity of metallized surfaces at terahertz frequencies," *Applied Physics Letters*, vol. 98, no. 17, p. 171912, 2011.

[35] E. Hammerstad and O. Jensen, "Accurate models for microstrip computer-aided design," *IEEE MTT-S International*, vol. 96, 1980.

[36] J. Qing and M. Navarro-Cía, "Loss and dispersion limitations of thz surface wave links," in *2023 48th International Conference on Infrared, Millimeter, and Terahertz Waves (IRMMW-THz)*, 2023, pp. 1–2.

[37] ——, "Capacity and energy efficiency of terahertz surface wave interconnects," 2023, accepted in Advanced Photonics Research.

Suzanna Freer received the M.Sc. degree in physics from The University of Sheffield, Sheffield, U.K., in 2018, and the Ph.D. degree from University of Birmingham, Birmingham, U.K, in 2022.

Her current research interests include terahertz (THz) imaging, evanescent fields, and spoof surface plasmon platforms.

She was a recipient of the Margaret K B Day Academic Award for academic excellence in research on Terahertz Evanescent Field Imaging and Sensing for Biological Applications – The British Federation of Women Graduates (2021).

Stephen M. Hanham (S'03–M'10) received the B.E. and B.Sc. degrees from The University of Western Australia, Perth, WA, Australia, in 2004 and the Ph.D. degree from The University of Sydney, Sydney, NSW, Australia, in 2010.

From 2008 to 2010, he was a Research Project Officer and Systems Engineer with the Commonwealth Scientific and Industrial Research Organization (CSIRO) in Sydney, Australia working on THz antennas and detectors, mobile satellite terminals and radio telescope antenna systems. From 2010 to 2017, he was a Postdoctoral Research Associate and later Experienced Researcher with Imperial College London, U.K. He is currently a Senior Birmingham Fellow and Associate Professor with the University of Birmingham, Birmingham, U.K. His research interests include electromagnetics, plasmonics, nano-materials, antennas and terahertz, and microwave technologies.

Jie Qing received the master's degree and Ph.D. degree from the University of Electronic Science and Technology of China, Chengdu, China, in 2017 and 2023, respectively. He is currently with the Terahertz Science and Technology Research Center, University of Electronic Science and Technology of China. His research interests include millimeter wave or THz devices and high power microwave technique and their applications.

Miguel Navarro-Cía (S'08–M'10–SM'15) received the MEng and PhD degrees in Telecommunication Engineering, and MRes degree in Introduction to Research in Communications from the Universidad Pública de Navarra, Spain, in 2006, 2010, and 2007, respectively.

From 2006 to 2010, he was a Pre-Doctoral Researcher, FPI Fellowship recipient, with the Electrical and Electronic Engineering Department, Universidad Pública de Navarra, where he was also a Research and Teaching Assistant from 2010 to 2011. Between 2008 and 2011, he also held several Visiting Researcher positions at the Valencia Nanophotonics Technology Center, Spain, Imperial College London, UK, and University of Pennsylvania, USA. He was a Research Associate in 2011 and a Junior Research Fellow from 2012 to 2015 at Imperial College London, UK. Between these two positions, he was a Research Associate with University College London, UK, where thereafter held a Visiting Researcher position until 2018. He is currently a Reader in TeraHertz Science and Engineering jointly with the School of Physics and Astronomy, and the School of Engineering, University of Birmingham, UK. He is also a Visiting Researcher with Imperial College London. His current research interests include theory, technology and applications of (near-field) time-domain spectroscopy/microscopy/imaging, metamaterials, plasmonics, antennas and frequency-selective surfaces at millimeter-wave, terahertz, and infrared.

Dr. Navarro-Cía is a Senior Member of the Optical Society of America and a member of the Institute of Physics and the European Optical Society. He was a recipient of the Best Doctoral Thesis in Basic Principles and Technologies of Information and Communications, and Applications corresponding to the XXXI Edition of Awards "Telecommunication Engineers" 2010, the CST University Publication Award (twice) for the best international journal publication using CST Microwave Studio in 2012 and 2016, and the 2011 Junior Research Raj Mittra Travel Grant.

Pavel Penchev received the B.Eng. degree in mechanical engineering and the Ph.D. degree in laser microprocessing from the University of Birmingham, Birmingham, U.K., in 2012 and 2016, respectively.

He was a Research Associate with the Laser Micromachining Group, Advanced Manufacturing Technology Center, University of Birmingham, from 2013 to 2015, where he has been a Research Fellow since 2015. His current research interests include the implementation of reconfigurable laser platforms for addressing challenging technological requirements of complex multilength scale products and the generic system-level tools and techniques for improving the machine tool performance of reconfigurable laser processing platforms in relation to their process reliability, flexibility, and robustness.

Stefan Dimov received the Diploma degree in engineering and the Ph.D. degree from the Moscow State University of Technology, Moscow, Russia, in 1984 and 1989, respectively, and the D.Sc. degree from Cardiff University, Cardiff, U.K., in 2011.

He is currently a Professor of micro manufacturing and the Head of the Manufacturing Research Group with the School of Engineering, University of Birmingham, Birmingham, U.K. He has authored over 250 articles and coauthored two books. His current research interests include the wider areas of micro and advanced manufacturing technologies.